Multiscale characterization of glass wools using X-ray micro-CT

Redouane Meftah[a,b,*], Sylvain Berger[b], Gary Jacqus[b], Jean-Yves Laluet[b], Veerle Cnudde[a,c]

[a] UGCT – PProGRess, Department of Geology, Ghent University, Krijgslaan 281/S8, 9000 Ghent, Belgium
[b] Saint-Gobain Research Paris, Department of Optics Metrology and Mathematics, 39 Quai Lucien Lefranc, 93300 Aubervilliers, France
[c] Chairholder "Porous media imaging techniques", Department of Earth Sciences, Utrecht University, Princetonlaan 8a, 3584CB Utrecht, the Netherlands

ARTICLE INFO

ABSTRACT

Glass wool is a fibrous material with many applications in construction. The present work compares the acoustic properties of two types of glass wool – a dense and less dense one. A combination of X-ray micro-CT and simulation was used to characterize the pore structure and acoustic behavior respectively. Based on high-resolution images, we were able to non-destructively achieve quantitative 3D information on the pore network and characteristics of fibers inside glass wool. Compared to experimental measurements, it is shown that better results are obtained with scans at 1 µm/voxel, especially on fibers diameter and characteristics lengths.

1. Introduction

Porous materials are commonly used in the field of construction or transport, especially for their acoustic and thermal properties [1]. Although found in nature, most porous materials used in construction are man-made and require an industrial process. These materials typically consist of a solid phase, called "skeleton", and a fluid phase. The composition of the raw materials that constitute the solid part are varied and often represent only 1 to 10% of the total volume of the material. In most cases, the fluid in question is air and is the most important part of the material. There are two main families of porous materials: those with a network of open interconnected pores and those with closed porosity, where the air is trapped in cavities within the material. Additionally, these porous materials can have a different nature (e.g. granular, fibrous, foams) and are presented in different forms (e.g. panels, rolls). Open porosity materials are frequently used to dissipate acoustic energy [2]. When they are directly exposed to acoustic waves, it is their sound absorption that differentiates them from other insulating materials. When the solid phase consists of fibers, their origin can vary largely. These fibers could be of animal (e.g. wool of sheep) [3], vegetable (e.g. wood fibers, straw) [4], mineral (e.g. glass wool, stone wool) [5] or synthetic (e.g. fiber of polyester) [6] origin. Based on the selected raw material, the manufacturing processes and constraints are different as well as the approach to optimize the performance of the material.

Mineral wools are probably the most common fibrous materials in the building industry. Additionally, they are also widely used in the field of transportation. Their acoustic performance concerns both insulation and/or sound absorption, depending on the application targeted [2,7]. There is a very wide range of commercial mineral wool available with different characteristics in thickness, density and acoustic performance. At the microscopic scale, glass fibers behave as an isotropic solid material. They have a density close to glass (2500 kg/m^3) [8]. The fibers' diameters are generally not homogeneous; they are commonly between 2 µm and 20 µm [9]. The binders used can modify the characteristics of the structure at the microscopic scale (e.g. fibers bound together, resin cluster …) and at the macroscopic scale (e.g. coloration). Glass wool is a heterogeneous material with a transverse and isotropic behavior at the macroscopic scale [10], because during the manufacturing process, the fibers are deposited in a stack of layers and thus form a structure with different properties depending on the direction [11]. In addition, glass fibers are distributed randomly and can introduce local changes in density.

In the last decade, high-resolution X-ray micro-CT has gained abundant attention in the 3D characterization of materials [12–14]. In several studies, especially in the field of textile research where the main parts of the structure are fibers, the yarn direction has been estimated with X-ray micro-CT [15–19]. In order to have access to data on the distribution of fibers, the most important step is the individual fiber segmentation [20–22]. Several studies have addressed the characterization of the pore network of fibrous porous media from a 3D image [23,24]. Compared to the extraction of pore networks in geo-materials [25,26], the main challenge for fibrous porous media consists in the extraction of their pores and throats. As for certain materials, including rocks, the distinction of pores and throats is often more obvious than in fibrous media. This is due to the complexity of the fibrous media and

---

* Corresponding author at: UGCT – PProGRess, Department of Geology, Ghent University, Krijgslaan 281/S8, 9000 Ghent, Belgium.
  E-mail address: Redouane.Meftah@UGent.be (R. Meftah).

the difficulty to segment the data. Few approaches using the watershed segmentation in pore network extraction of fibrous media were carried out [27,28].

Soltani et al. [29] carried out a similar work on melt-spun polypropylene fibers of different fineness and same density. They observed that the sound absorption coefficient was higher in sample with the lowest finesse at all frequency range.

In this study, glass wools with different densities are studied in order to investigate the mechanisms related to the acoustic dissipation and specifically the role played by the microstructure. To examine this, the materials were scanned on two micro-CT systems, allowing the study of the 3D microstructure and the extraction of the intrinsic parameters. Fiber characteristics could be determined accurately, by performing 3D analysis on the high micro-CT images. These images also allow for fluid flow simulation through the pore structure, adding to the understanding of the microstructure role. We thus provide direct information on the acoustic behavior based on 3D images.

2. Theory

2.1. Micro-CT

X-ray micro-CT is a non-destructive technique that provides a three-dimensional image. As such, it allows to better describe the physical phenomena occurring at the local scales and their influence on the properties. Since the 1970s, this technique has been developed and used in the medical field. The spatial resolution was then not very good, around 300 μm. Thanks to the development of new technologies in computer science and optics, a resolution below the micron can be reached today [30].

Like a medical examination scanner, X-rays are used in micro-CT to acquire radiographs of the object under observation. The principle of acquiring radiographs is shown schematically in Fig. 1. X-rays are generated by an X-ray source, transmitted through an object, and recorded by a detector as a 2D projection image (Fig. 2a). The sample is mounted on a rotational stage and then rotated over 360° to take an image at each rotation step.

The image obtained is called radiography as shown in Fig. 2a. This is the result of the radiation transmitted through the material. Indeed, the material absorbs a part of the X-rays differently depending on its components. The gray levels obtained on each acquired projection characterize the absorption capacity of the various components. X-rays and materials have different mechanisms: photoelectric absorption, coherent scattering (photon absorbed by an atom ad re-emitted with the same energy), and incoherent scattering (photon interacting with an electron of the material, transferring a part of its energy and the rest is transmitted to a diffused photon). The different types of interactions coexist in proportions depending on the energy of the X-rays and the nature of the material investigated and are visualized by the gray levels of the projection captured (Fig. 2a).
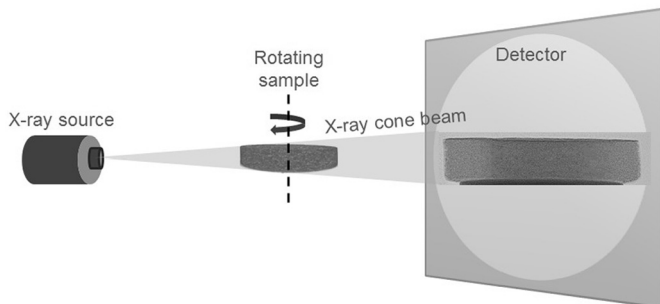

Fig. 1. A lab-based micro-CT setup with the X-ray tube focal spot, producing conical X-rays, a sample mounting on a rotation stage and the X-ray detector.

2.2. Acoustic theory

In the following it is assumed that the porous skeleton is motionless (no coupling between fluid and solid phase) and one is interested in describing the behavior of a compression wave propagating inside an equivalent fluid.

In air, the propagation of acoustic waves is characterized by the characteristic impedance Z_0 and the wave number k_0. These parameters depend on the density ρ_0 and the bulk modulus of air K_a. Under these conditions, the losses are neglected and ρ_0 and K_a are real quantities (not complex). In the case of porous materials, the air saturates a complex microstructure. The loss phenomena by viscous and thermal dissipation are then no longer negligible. The characteristic impedance and the wavenumber of the fluid become complex functions that depend on the frequency. These functions describe the propagation of acoustic waves through an effective fluid whose intrinsic characteristics are homogenized on a macroscopic scale. These considerations are valid in the case where the acoustic wavelength is large compared to the dimensions of the microstructure.

In general, the models focus on determining the effective density $\widetilde{\rho}_{eff}$ and the effective bulk modulus $\widetilde{K}_{eff}$, or the complex characteristic impedance $\widetilde{K}_c$ and the complex wavenumber $\widetilde{k}$. For the rest of the study, we determine:

- The equivalent density $\widetilde{\rho}_{eq} = \widetilde{\rho}_{eff}/\varphi$ and the normalized equivalent density $\widetilde{\rho}_{eq\_n} = \widetilde{\rho}_{eff}/\rho_0$ where φ is the porosity of the material and ρ_0 is the density of air
- The equivalent bulk modulus $\widetilde{K}_{eq} = \widetilde{K}_{eff}/\varphi$ and the normalized bulk modulus $\widetilde{K}_{eq\_n} = \widetilde{K}_{eff}/P_0$ where φ is the porosity of the material and P_0 is the atmospheric pressure.

The characteristic impedance and the wavenumber are linked to the equivalent density and the equivalent bulk modulus as follows:

$$\widetilde{K}_c = \sqrt{\widetilde{\rho}_{eq}\widetilde{K}_{eq}}; \widetilde{k} = \omega\sqrt{\widetilde{\rho}_{eq}/\widetilde{K}_{eq}}$$

The structure of real porous materials is complex and requires the use of simplified models to determine the equivalent bulk modulus and density functions. Several approaches are available: empirical, analytical and semi-phenomenological.

Subsequently, the approach adopted will be semi-phenomenological. It has the advantage to adapt the complexity of materials by homogenizing its properties using macroscopic parameters. This is not possible with analytical modeling because it requires precise knowledge of the geometry of the microstructure, which is possible only for limited and idealized microstructures [31]. Moreover, the parameters used in a semi-phenomenological approach are sufficiently detailed and precise to give an understanding of the role of the microstructure, unlike the empirical models that mask certain physical phenomena.

It is generally accepted in the scientific community that the Johnson-Champoux-Allard (JCA) model [32] is a good trade off to describe the acoustic behavior of porous media.

The macroscopic parameters of this model can all be measured and are common to a wide range of porous materials. They do not all have the same area of influence on the spectrum and their values are more or less dependent on each other in reality. The diversity of microstructures (granular, fibrous, foam, etc.) also induces significant differences from one material to another. The parameters that constitute the JCA model are the porosity, the resistivity, the tortuosity, the viscous and thermal characteristics lengths. In this model, the dynamic density [33] of an acoustical porous material is expressed as:

$$\widetilde{\rho}_{eq}(\omega) = \frac{\alpha_\infty\rho_0}{\varphi}\left[1 + \frac{\sigma\varphi}{j\omega\rho_0\alpha_\infty}\sqrt{1 + \frac{4\alpha_\infty^2\eta\rho_0\omega}{\sigma 2\Lambda 2\varphi 2}}\right]$$

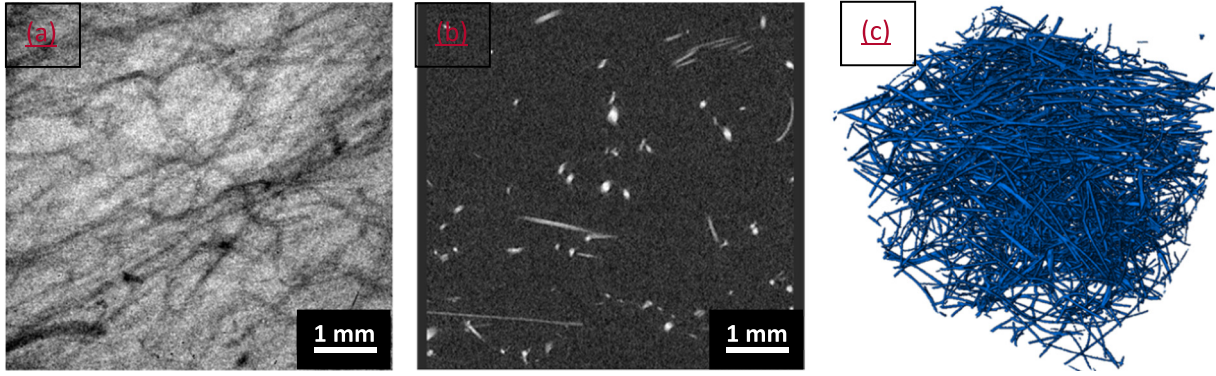where the open porosity φ, the static air flow resistivity σ, the high

Fig. 2. Glass wool sample: (left) X-ray projection (center) tomographic section after reconstruction (right) 3D rendering.

frequency limit of the torotuosity α_∞, the viscous characteristic length Λ, and the kinematic viscosity of air η are involved. On the other hand, the dynamic bulk modulus [34] can be expressed as:

$$\widetilde{K}_{eq}(\omega) = \frac{\gamma P_0 / \varphi}{\gamma - (\gamma-1)\left[1 - j\frac{8K}{\Lambda'^2 C_p \rho_0 \omega}\sqrt{1 + j\frac{\Lambda'^2 C_p \rho_0 \omega}{16K}}\right]^{-1}}$$

where the open porosity φ and the thermal characteristic length are involved. Note that other model exist in the literature [35,36]. They will not be described in this paper because the parameters that constitute them are not always related to physical quantities linked to the microstructure. Moreover, their experimental determination can be tricky.

3. Materials and methods

3.1. Glass wools

Two glass wools named 406 and 409 (Fig. 3) with different characteristics were studied, and whose related manufacturing process characteristics were carefully selected throughout a pilot campaign [9]. Table 1 presents the characteristics of the glass wools and the factory parameters used for manufacturing the samples.

In a $100 \times 100 \times 30$ mm^3 panel, glass wool plugs perpendicular to the length of the fibers were prepared using a core drill bit (15 mm diameter and 30 mm length). For each specimen of glass wool, three individual plugs were taken. In addition, five other small samples (1 mm diameter and 3 mm length) were taken and cut perpendicular to the length of the fibers with a cuter (Fig. 3c) from each specimen.

3.2. X-ray micro-CT

To establish the link between the macroscopic acoustic properties of

Table 1
Characteristics of the samples.

Reference	Thickness [mm]	Density [kg/m^3]
406	30	20
409	33	80

the glass wools and the microscopic characteristics, a high resolution X-ray micro-CT was performed at HECTOR [37], the high-energy scanner of the Ghent University Centre of X-Ray Tomography (UGCT) and at Medusa [38], the high resolution scanner of UGCT (Fig. 4). The samples were scanned at several resolutions, 3.5 µm/voxel and 1 µm/voxel. The scanning parameters are given in Table 2. The tomographic images were reconstructed with the Octopus reconstruction software [39]. The sizes of the full scans at 3.5 µm and 1.0 µm were $2000 \times 2000 \times 1723$ voxels^3 and $691 \times 691 \times 576$ voxels^3 respectively.

Avizo® 3D software was used for image analysis and generation of meshes.

3.3. Simulation

ScalingCell was used for the simulation of the macroscopic behavior of porous materials from their microstructure. This software links the 3D micro-morphology of a porous material to its vibro-acoustic properties. In this study, *ScalingCell* was used to determine the thermal and viscous characteristics lengths. Two approaches are implemented in *ScalingCell*. The first one comprises considering the real material microstructure extracted from X-ray micro-tomography. The second one uses an idealized, generic representation of the microstructure. We will focus on the real structure of glass wool. For simulations, *ScalingCell* uses FreeFem + +, which is an efficient partial differential equation solver, coupled to a hybrid method. This method solves the local
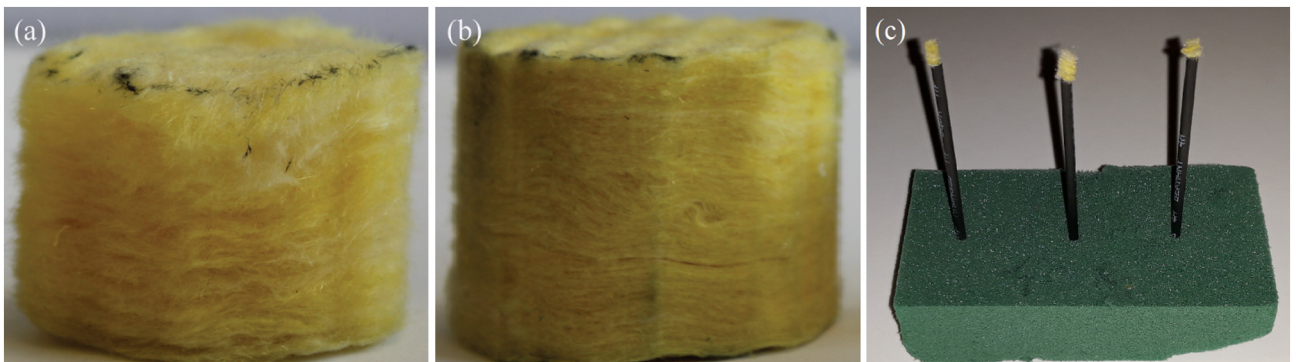

Fig. 3. Macroscopic pictures of the glass wools (diameter = 15 mm, length = 30 mm) (a) sample 406 (b) sample 409 (c) small samples mounted on graphite sticks.
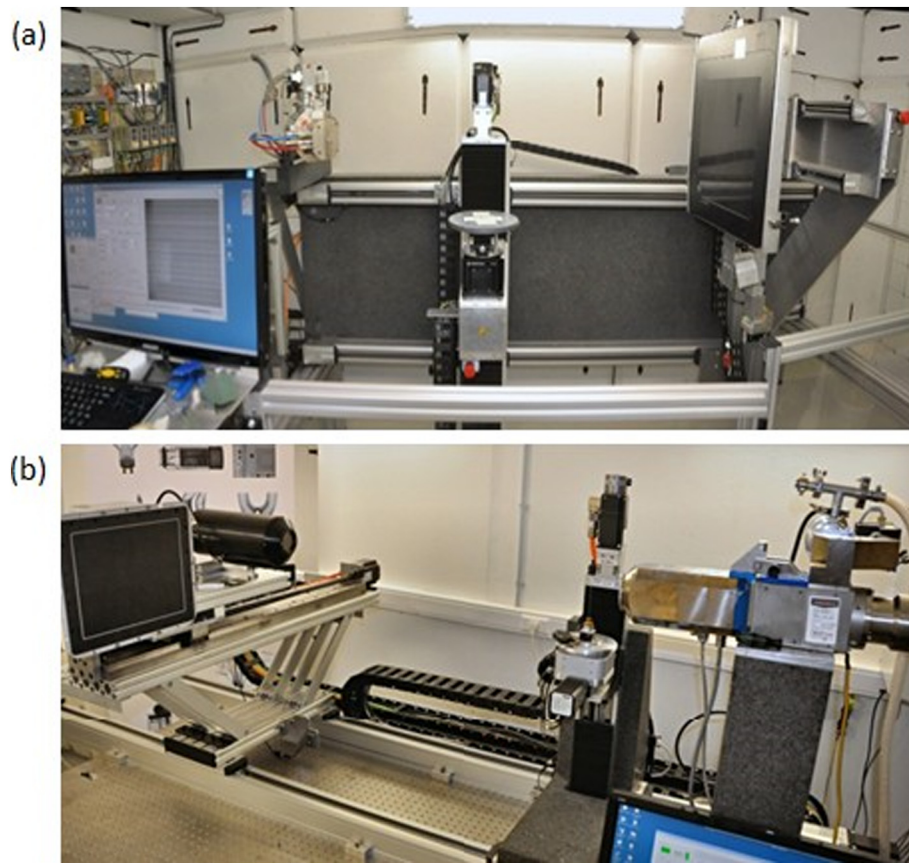
Fig. 4. Micro-CT apparatus at UGCT (a) HECTOR [37] (b) Medusa [38].

equations governing the asymptotic frequency-dependent visco-thermal dissipation phenomena on the proposed elementary cell [40]. To compute the acoustical properties of glass wool the Johnson-Champoux-Allard model was used (see Theory section).

4. Results and discussion

4.1. Pore network characterization

Fig. 5 illustrates the obtained micro-CT data of the glass wools at different resolutions. In these reconstructions the difference of density can be clearly distinguished. We can see more fibers in sample 409, which appear to be longer.

4.1.1. Determination of porosity, air flow resistivity and tortuosity

The segmentation of the pore space and the fibers was based on a region growing method. The global porosity was computed on segmented data by counting the voxels.

The XLab simulation extension within Avizo® allows calculating absolute permeability. It computes the absolute permeability tensor by solving the Stokes equations and Darcy's law. The specifications are: Newtonian fluid, incompressible fluid, single-phase fluid (relative permeability not addressed) and impermeable solid phase. In this study, this was used to calculate the air flow resistivity $= \mu_{air}/K_{zz}$, where μ_{air} is

the dynamic viscosity of air (1.48×10^{-5} Pa·s at 20 °C) and K_{zz} transverse absolute permeability in m^2.

Tortuosity is defined as the ratio between the length of the path and the distance between its ends along the z-axis. In our case the distance between the ends of curve is given by the number of planes along z-axis. Avizo first computes the centroid of segmented pores for each horizontal slice of the image. Then it computes the path length through the centroids, after which it divides it by the number of slices along the z-axis.

Table 3 summarizes the results from the image analysis. The average values and their standard deviations over five samples are presented for the scans at 1 μm/voxel and three samples for the scans at 3.5 μm/voxel.

For sample 406, the entire 3D pore space consists out of 0.986 and 0.982 for the low and high resolution scans respectively. Since the standard deviation is very small and porosity values for both resolutions are the same, we can deduce that the subsamples are homogeneous in their porosity value. For sample 409, we note a difference of 0.02 in porosity between the two scans, which corresponds to a relative difference of 2.2%. As this is a negligible difference, we deduce that sample 409 is also homogenous in porosity. We logically observe that sample 409 is less porous than sample 406 because it is denser. Glass wool 409 is dramatically more resistive than 406. This high resistivity value has to be linked with the higher density and of the product.

Table 2
Scanning parameters.

Micro-CT system	Source voltage (keV)	Output power (W)	Number of projections	Scan time (min)	Resolution (μm/voxel)
HECTOR	160	10	2201	42	3.5
Medusa	70	1	1050	27	1.0
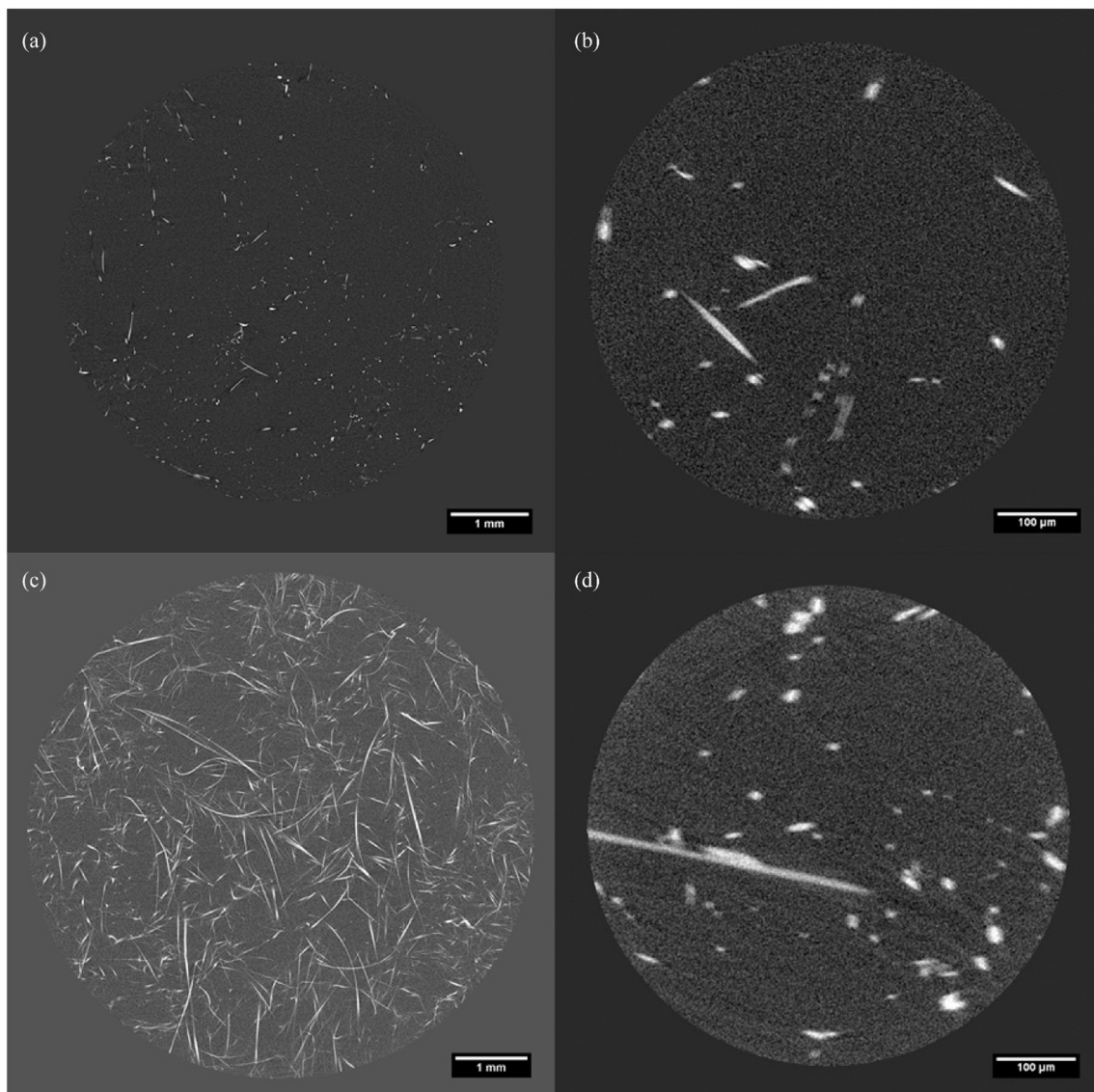
Fig. 5. 2D reconstructed slices of sample 406 at 3.5 μm/voxel (a) and at 1.0 μm/voxel (b) and sample 409 at 3.5 μm/voxel (c) at 1 μm/voxel (d).

Tortuosity is slightly higher for sample 409 than sample 406. Indeed, when the material is denser the path becomes more tortuous as it becomes harder to find a straight path.

4.1.2. Determination of representative elementary volume

The representative elementary volume (REV) is the determination of the smallest volume for which the pore network represents a larger sample. The choice of REV has to satisfy certain criteria: in this case it has to contain enough pores to have a significant global average. In a small volume, the fluctuations of porosity will be associated to the microstructure and in a large volume, variations will be due to the macroscopic structure.

The REV for porosity was determined by taking 50 cubic subsamples

in the center, with increasing size. The cube dimensions were expended symmetrically in all directions from a 1x1x1 voxels^3 cube starting point. The maximum volume for the cube was determined by the radius of the cylinder ($L_{\max} = \frac{2R}{\sqrt{2}}$ where $L_{\max} = (V_{\max})^{1/3}$). For each single cube, the porosity was computed. The representative elementary volume was obtained when the porosity became stable.

Fig. 6 shows the REV analysis for porosity of the glass wools at high and lower resolution. The x-axis represents the volume of the subsamples. As shown in Fig. 6, we can observe two regions: 1) the first region represents at "small" scales random fluctuations due to the microscopic structure; associated with pore scale heterogeneity; 2) the left-hand boundary of the second region shows a minimum REV where the porosity values are scale-independent and precisely represent a

Table 3
Results from 3D image analysis.

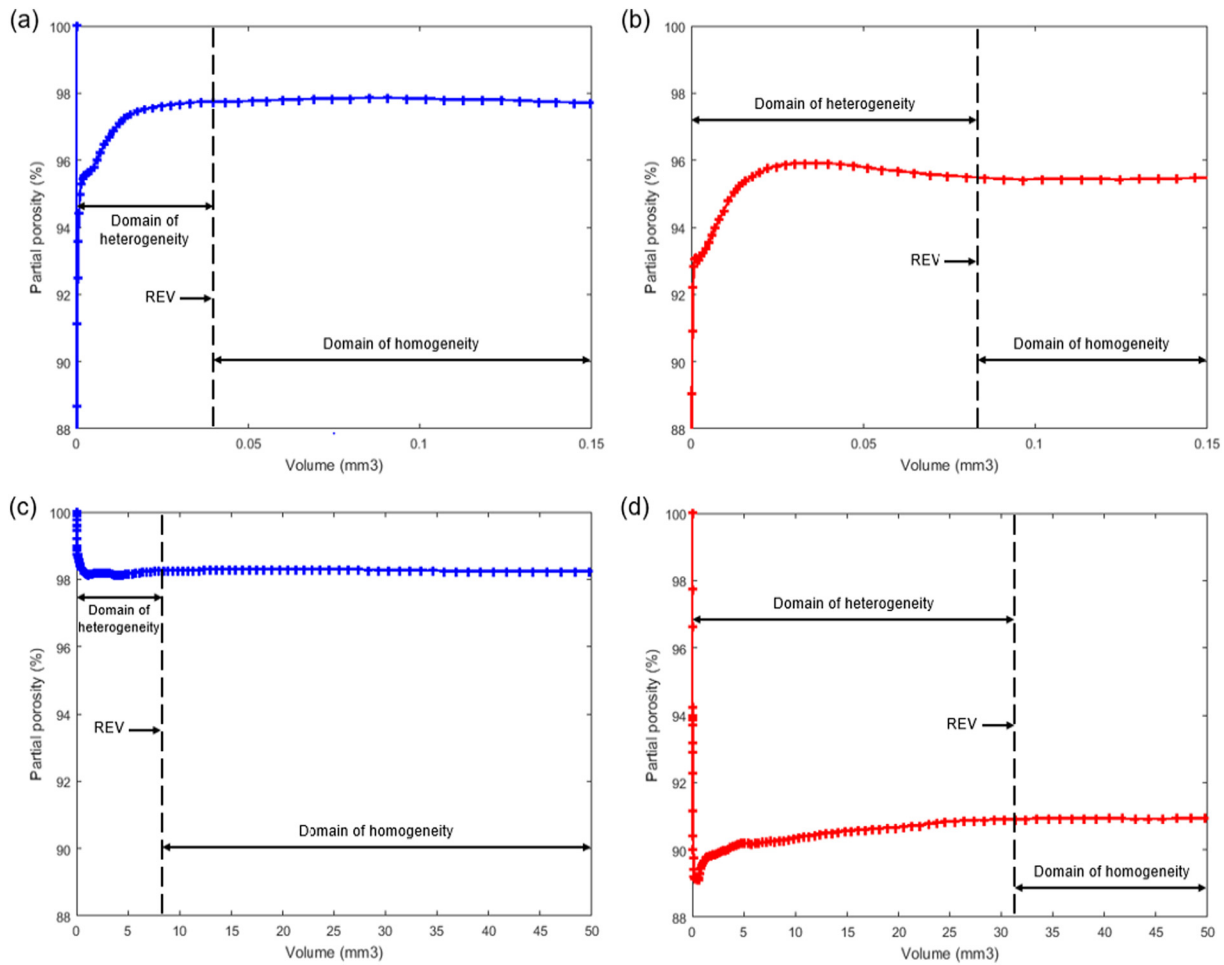| Sample	Porosity [–]		Air resistivity [Pa·s·m^{-2}]		Tortuosity [–]	
	3.5 μm	1.0 μm	3.5 μm	1.0 μm	3.5 μm	1.0 μm
406	0.986 ± 0.009	0.982 ± 0.002	9457 ± 1210	14,340 ± 1700	1.01 ± 0.01	1.01 ± 0.01
409	0.943 ± 0.011	0.964 ± 0.007	72,260 ± 4540	83,420 ± 3500	1.09 ± 0.03	1.01 ± 0.01

Fig. 6. Determination of REV for porosity of sample 406 at 1.0 μm/voxel (a) sample 409 at 1.0 μm/voxel (b) and sample 406 at 3.5 μm/voxel (c) sample 409 at 3.5 μm/voxel (d).

larger sample.

From the graphs, we can observe that the REV is resolution dependent. The porosity data indicates a REV of 0.04 mm^3 and 8 mm^3 for sample 406 at 1.0 μm/voxel and 3.5 μm/voxel, respectively. These volumes represent a cubic sample of $0.34 \times 0.34 \times 0.34$ mm^3 and $2 \times 2 \times 2$ mm^3 respectively. Concerning sample 409, the porosity data indicates a REV of 0.085 mm^3 and 31 mm^3 at 1.0 μm/voxel and 3.5 μm/voxel, respectively. At both resolutions, the REV for the least dense sample is smaller than for the densest sample. This is because there are more fibers in sample 409 and this creates more heterogeneity in the volume.

4.1.3. Determination of thermal and viscous characteristic length

From the segmented X-ray CT images, meshes of the real microstructures were extracted with Avizo® 3D software. To avoid very long computation times, the simulations were done on a sub-volume that was defined from the REV to compute the viscous characteristic length. This corresponds to a volume of $700 \times 700 \times 700$ voxels^3 for scans at 3.5 μm/voxels, and a volume of $450 \times 450 \times 450$ voxels^3 for scans at 1.0 μm/voxel. The thermal characteristic length is a geometrical parameter defined as the hydraulic radii of pores. The viscous characteristic length is computed in high frequency limit assuming an inviscid fluid [40].

Triangle meshes with 10,000 points and 19,000 faces were used for the simulation. Fig. 7 represents a zoomed part of the mesh for sample 409 at the resolution 1.0 μm/voxel. Table 5 presents the results from the acoustic simulations.
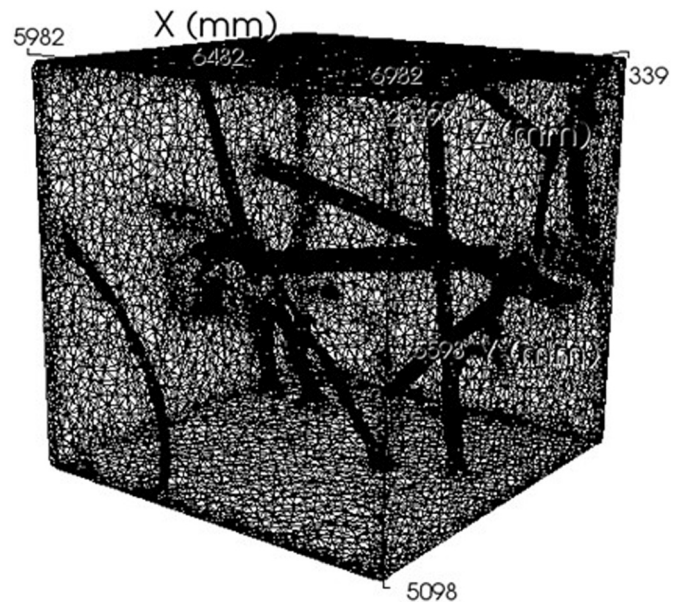

Fig. 7. Mesh for sample 409.

The viscous characteristic length controls the viscous effects at medium and high acoustical frequencies and is related to the size of the inter-connection between two pores. Conversely, the thermal
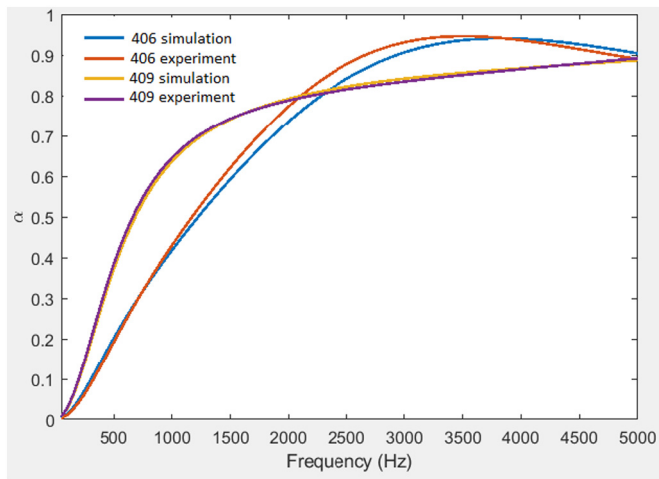
Fig. 8. Normal sound absorption coefficient spectra for sample 406 and 409 - The JCA model was used for a frequency range between 50 Hz and 5000 Hz with a 50 Hz step.

characteristic length describes the thermal effects at medium and high acoustical frequencies and is related to the largest size of the pores. By comparing sample 406 and sample 409, it is found that the viscous characteristic length for sample 406 is 1.7 times larger than that for sample 409. It was also found that the thermal characteristic length for sample 409 is 0.76 times smaller than that for sample 406.

Fig. 8 shows the simulated normal sound absorption coefficient spectra for the two types of glass wool and the experimental one carried out by Kerdudou et al. [9]. For the frequency range 50 Hz–2000 Hz, sample 409 has a better a higher sound absorption coefficient than sample 406 due to its higher airflow resistivity. The simulated normal sound absorption coefficient for sample 409 is in total agreement with the experimental measurement. For sample 406, we observed a slight difference between the simulated and experimental coefficient but the overall agreement is satisfactory.

4.2. Fibers analysis

The XFiber extension within Avizo® provides specific support for analyzing fibers. It includes many tools to compute advanced fiber statistics. Fig. 9 shows the 3D rendering of the fibers with Avizo® for the scans at 3.5 μm/voxel. The difference in density between the two

Table 4
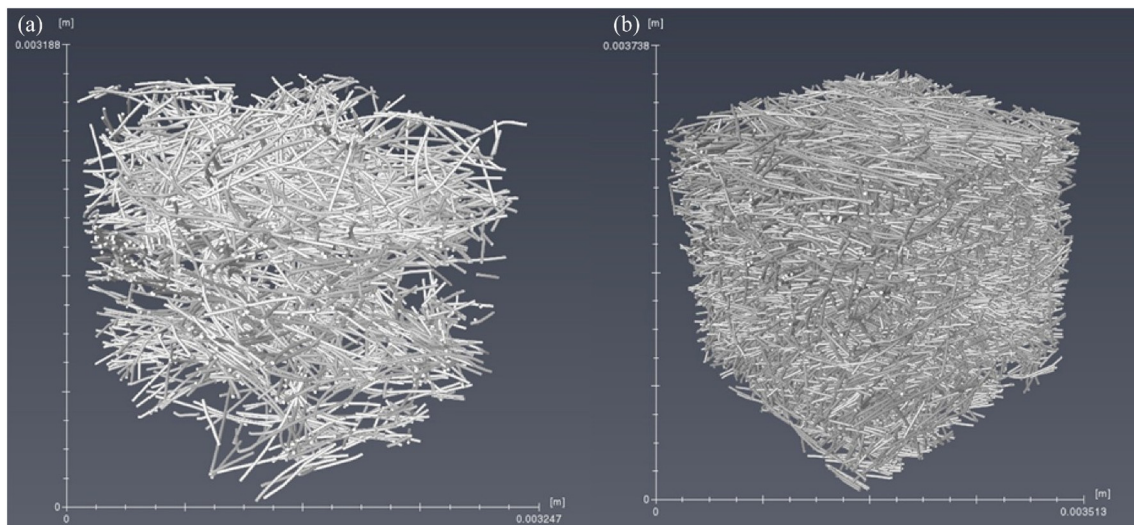Viscous and thermal characteristic lengths computed with *ScalingCell*.

Sample	Viscous length Λ [μm]		Thermal length Λ′ [μm]	
	3.5 μm	1.0 μm	3.5 μm	1.0 μm
406	154 ± 13	98 ± 10	210 ± 20	190 ± 9
409	90 ± 5	53 ± 9	160 ± 15	101 ± 8

samples is very well observed. The fibers in sample 409 appear more compact than those in samples 406.

We extracted the mean and median values of the fiber diameters for each scan (Table 4). For sample 406, the mean values are 9.3 μm and 5.4 μm for scans at 3.5 μm/voxel and 1.0 μm/voxel, respectively. For sample 409, the mean values are respectively 12.8 μm and 4.3 μm. For the high-resolution scan the mean values are smaller. This is because the high-resolution scan allows to image fibers that are below the scan resolution of 3.5 μm/voxel. Furthermore, between the two samples the mean values are almost identical. The special interest of determining the median fiber diameter is that it can be used for analytical models such as those of Tarnow [41,42] to estimate the resistivity from average fiber diameter or it can be used as input data for models to generate idealized fibrous cells [43]. Tarnow showed that the airflow resistivity is inversely proportional to the square of the fiber radius when the concentration of fibers is constant.

4.3. Comparison with experimental results

Experimental work was carried out by Kerdudou et al. [9] on similar glass wools, with the aim to link macroscopic parameters to the microstructure of the fibrous materials. The results of these experiments were used here to validate our approach with micro-CT. Fig. 10 presents a comparison between the experimental and computational results for the intrinsic and acoustic parameters. Excellent agreement was found between the experimental and numerical results for porosity, air resistivity and tortuosity. Compared to experimental values, the 3.5 μm/voxel scans give the same trends as the 1 μm/voxel scans for these parameters. A high-resolution scan does not give more information.

Regarding the mean values of fiber diameters: for the scans at 3.5 μm/voxel we have 12.8 μm for sample 409 and 9.3 μm for sample 406. Experimental values are 4.6 μm and 5.4 μm for samples 409 and 406, respectively. At this resolution, the mean fiber diameters were overestimated. This is explained by that fibers are located on 1 or 2

Fig. 9. 3D rendering of fibers with Avizo® (a) sample 406 at 3.5 μm/voxel (b) sample 409 at 3.5 μm/voxel.

Table 5
Microstructure data measurements.

	Fiber diameter (µm)			
	Median		Mean	
Scan resolution	3.5 µm/voxel	1 µm/voxel	3.5 µm/voxel	1 µm/voxel
406	9.0	4.2	9.3	5.4
409	11.8	3.4	12.8	4.3

voxels at this resolution. Also, there are edge effects that make fibers look thicker than they actually are. Results from the scans at 1 µm/voxel give excellent agreement with experimental values.

Our simulated values for the viscous and thermal characteristic lengths were overestimated for both resolutions. However, the results given by high-resolution scans are much more accurate than those given by low resolution scans.

5. Conclusion

This work shows the method of combination of micro-CT and simulation to investigate the link between intrinsic parameters and acoustical performance of two real glass wools with different densities.
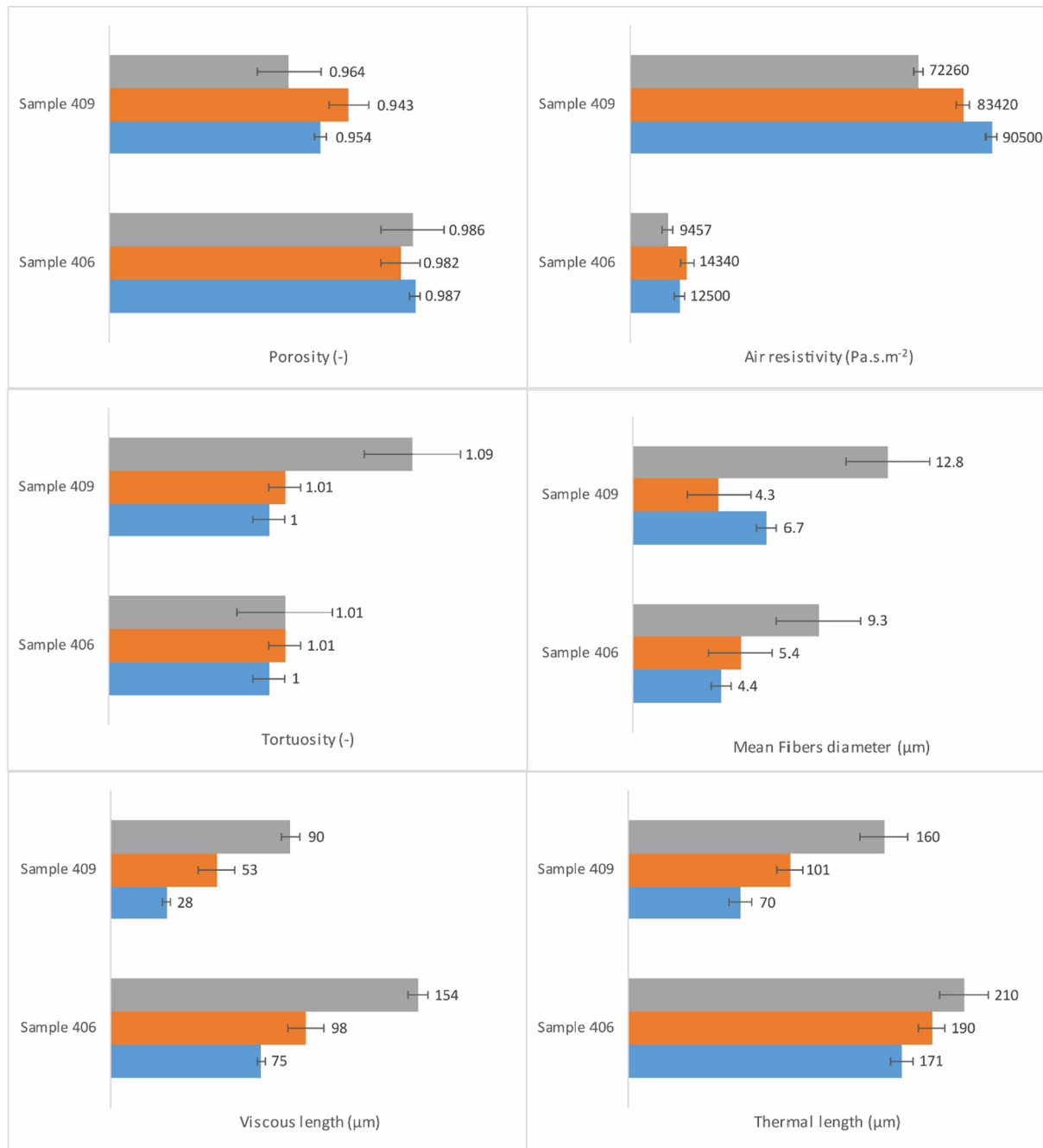

Fig. 10. Intrinsic and acoustic parameters for samples 406 and 409. Left panel: porosity, tortuosity and viscous length (from top to bottom). Right panel: air resistivity, mean fibers diameter and thermal length (from top to bottom). Colors: experimental data Kerdudou et al. [9] (blue), scan at 1 µm (orange) and scan at 3.5 µm (gray). (For interpretation of the references to color in this figure legend, the reader is referred to the web version of this article.)

The main challenge of this work is to provide a full characterization at both microscopic and macroscopic scales of real fibrous materials with micro-CT in order to calculate intrinsic parameters and understand the acoustical absorption of glass wools.

The Johnson-Champoux-Allard has been used to predict the acoustic properties of glass wools. Close fit, between experimental data and the predictions from image analysis and acoustic simulation, has been observed. It has been found that the scans at 1 μm/voxel give more accurate results by comparing them with experimental measurements, especially on fiber diameters and characteristic lengths. In addition, a REV was found at this resolution. Further investigation of the influence of the fibers (orientation, heterogeneity) on the acoustic properties is needed to provide an added value for this work.

Data availability

The raw and processed data required to reproduce these findings cannot be shared at this time due to legal reasons.

Declaration of competing interest

There is no conflict of interest.

Acknowledgments

References

[1] S. Rashidi, J.A. Esfahani, N. Karimi, Porous materials in building energy technologies—a review of the applications, modelling and experiments, Renew. Sust. Energ. Rev. 91 (2018) 229–247. Aug.

[2] K.O. Ballagh, Acoustical properties of wool, Appl. Acoust. 48 (2) (1996) 101–120 Jun.

[3] A.B. Wildman, The identification of animal fibres, J. Forensic Sci. Soc 1 (2) (1961) 115–119 Mar.

[4] S. Panthapulakkal, M. Sain, The use of wheat straw fibres as reinforcements in composites, Biofiber Reinforcements in Composite Materials, Elsevier, 2015, pp. 423–453.

[5] B. Širok, B. Blagojević, P. Bullen, B. Širok, B. Blagojević, P. Bullen, Introduction, Mineral Wool, Elsevier, 2008, pp. 1–7.

[6] J. Zach, R. Slávik, V. Novák, Investigation of the process of heat transfer in the structure of thermal insulation materials based on natural fibres, Procedia Eng 151 (2016) 352–359 Jan.

[7] F.R. Jones, N.T. Huff, The structure and properties of glass fibres, Handbook of Textile Fibre Structure, Elsevier, 2009, pp. 307–352.

[8] J. Willoughby, "Insulation," in Plant Engineer's Reference Book, Elsevier, 2002, pp. 30-1-30–18.

[9] P. Kerdudou, J.-B. Chéné, G. Jacqus, C. Perrot, S. Berger, P. Leroy, A semi-empirical approach to link macroscopic parameters to microstructure of fibrous materials, InterNoise, 2015.

[10] R. Gellert, Inorganic mineral materials for insulation in buildings, Materials for Energy Efficiency and Thermal Comfort in Buildings, Elsevier, 2010, pp. 193–228.

[11] J. Mountifield, Forming processes for glass fibre and resin—other methods, Composites 1 (1) (1969) 41–49 Sep.

[12] J.-Y. Buffiere, E. Maire, J. Adrien, J.-P. Masse, E. Boller, In situ experiments with X ray tomography: an attractive tool for experimental mechanics, Exp. Mech. 50 (3) (Mar. 2010) 289–305.

[13] H. Tran, P. Doumalin, C. Delisee, J.C. Dupre, J. Malvestio, A. Germaneau, 3D mechanical analysis of low-density wood-based fiberboards by X-ray microcomputed tomography and digital volume correlation, J. Mater. Sci. 48 (8) (2013) 3198–3212. Apr.

[14] G. Gaiselmann, I. Manke, W. Lehnert, V. Schmidt, Extraction of curved fibers from 3D data, Image Anal. Stereol 32 (1) (2013) 57 Mar.

[15] X. Thibault, J.-F. Bloch, Structural analysis by X-ray microtomography of a strained nonwoven papermaker felt, Text. Res. J. 72 (6) (2002) 480–485 Jun.

[16] P. Badel, E. Vidal-Sallé, E. Maire, P. Boisse, Simulation and tomography analysis of textile composite reinforcement deformation at the mesoscopic scale, Compos. Sci. Technol. 68 (12) (2008) 2433–2440 Sep.

[17] X. Zeng, L.P. Brown, A. Endruweit, M. Matveev, A.C. Long, Geometrical modelling of 3D woven reinforcements for polymer composites: prediction of fabric permeability and composite mechanical properties, Compos. Part A Appl. Sci. Manuf 56 (2014) 150–160 Jan.

[18] I. Straumit, S.V. Lomov, M. Wevers, Quantification of the internal structure and automatic generation of voxel models of textile composites from X-ray computed tomography data, Compos. Part A Appl. Sci. Manuf 69 (2015) 150–158 Feb.

[19] M. Amiot, M. Lewandowski, P. Leite, M. Thomas, A. Perwuelz, An evaluation of fiber orientation and organization in nonwoven fabrics by tensile, air permeability and compression measurements, J. Mater. Sci. 49 (1) (2014) 52–61 Jan.

[20] J.C. Tan, J.A. Elliott, T.W. Clyne, Analysis of tomography images of bonded fibre networks to measure distributions of fibre segment length and fibre orientation, Adv. Eng. Mater. 8 (6) (2006) 495–500 Jun.

[21] M. Couprie, S. Meulenyzer, M.A. Salem, H. Talbot, F. Pourcel, Fibre analysis in 3D materials and process validation on artificial data, J. Microsc. 255 (2) (May 2014) n/a-n/a.

[22] L. Chapelle, et al., Determination of the fibre orientation distribution of a mineral wool network and prediction of its transverse stiffness using X-ray tomography, J. Mater. Sci. 53 (9) (2018) 6390–6402 May.

[23] P. Bhattad, C.S. Willson, K.E. Thompson, Effect of network structure on characterization and flow modeling using X-ray micro-tomography images of granular and fibrous porous media, Transp. Porous Media 90 (2) (2011) 363–391 Nov.

[24] X. Huang, Y. He, W. Zhou, D. Deng, Y. Zhao, Pore network modeling of fibrous porous media of uniform and gradient porosity, Powder Technol. 343 (2019) 350–361 Feb.

[25] H. Dong, M.J. Blunt, Pore-network extraction from micro-computerized-tomography images, Phys. Rev. E 80 (3) (2009) 036307 Sep.

[26] T. Bultreys, L. Van Hoorebeke, V. Cnudde, Multi-scale, micro-computed tomography-based pore network models to simulate drainage in heterogeneous rocks, Adv. Water Resour. 78 (2015) 36–49. Apr.

[27] T. Agaesse, A. Lamibrac, F.N. Büchi, J. Pauchet, M. Prat, Validation of pore network simulations of ex-situ water distributions in a gas diffusion layer of proton exchange membrane fuel cells with X-ray tomographic images, J. Power Sources 331 (2016) 462–474 Nov.

[28] J.T. Gostick, Versatile and efficient pore network extraction method using marker-based watershed segmentation, Phys. Rev. E 96 (2) (2017) 023307. Aug..

[29] P. Soltani, M. Azimian, A. Wiegmann, M. Zarrebini, Experimental and computational analysis of sound absorption behavior in needled nonwovens, J. Sound Vib. 426 (2018) 1–18 Jul.

[30] J. Baruchel, et al., Advances in synchrotron radiation microtomography, Scr. Mater. 55 (1) (2006) 41–46 Jul.

[31] J.-F. Allard, Propriétés acoustiques des matériaux poreux saturés d'air et théorie de Biot, J. d'Acoustique 3 (1990) 29–38.

[32] J.F. Allard, N. Atalla, Propagation of Sound in Porous Media: Modelling Sound Absorbing Materials, Chichester, UK, John Wiley & Sons, Ltd, 2009.

[33] D.L. Johnson, J. Koplik, R. Dashen, Theory of dynamic permeability and tortuosity in fluid-saturated porous media, J. Fluid Mech. 176 (1) (Mar. 1987) 379.

[34] Y. Champoux, J. Allard, Dynamic tortuosity and bulk modulus in air-saturated porous media, J. Appl. Phys. 70 (4) (Aug. 1991) 1975–1979.

[35] D.K. Wilson, Relaxation-matched modeling of propagation through porous media, including fractal pore structure, J. Acoust. Soc. Am 94 (2) (1993) 1136–1145. Aug.

[36] K. Attenborough, Acoustical characteristics of rigid fibrous absorbents and granular materials, J. Acoust. Soc. Am 73 (3) (1983) 785–799 Mar.

[37] B. Masschaele, et al., HECTOR: a 240 kV micro-CT setup optimized for research, J. Phys. Conf. Ser. 463 (2013) 012012Oct.

[38] B.C. Masschaele, V. Cnudde, M. Dierick, P. Jacobs, L. Van Hoorebeke, J. Vlassenbroeck, UGCT: new X-ray radiography and tomography facility, Nucl. Instruments Methods Phys. Res. Sect. A Accel. Spectrometers, Detect. Assoc. Equip 580 (1) (2007) 266–269 Sep.

[39] J. Vlassenbroeck, M. Dierick, B. Masschaele, V. Cnudde, L. Van Hoorebeke, P. Jacobs, Software tools for quantification of X-ray microtomography at the UGCT, Nucl. Instruments Methods Phys. Res. Sect. A Accel. Spectrometers, Detect. Assoc. Equip 580 (1) (2007) 442–445 Sep.

[40] C. Perrot, F. Chevillotte, R. Panneton, Bottom-up approach for microstructure optimization of sound absorbing materials, J. Acoust. Soc. Am 124 (2) (2008) 940–948.

[41] V. Tarnow, Airflow resistivity of models of fibrous acoustic materials, J. Acoust. Soc. Am 100 (6) (1996) 3706–3713.

[42] V. Tarnow, Measured anisotropic air flow resistivity and sound attenuation of glass wool, J. Acoust. Soc. Am. 111 (6) (2002) 2735–2739 Jun.

[43] M. He, C. Perrot, J. Guilleminot, P. Leroy, G. Jacqus, Multiscale prediction of acoustic properties for glass wools: computational study and experimental validation, J. Acoust. Soc. Am 143 (6) (2018) 3283–3299 Jun.